



Location-Specific Microstructure Characterization Within IN625 Additive Manufacturing Benchmark Test Artifacts

M. R. Stoudt¹ · M. E. Williams¹ · L. E. Levine¹ · A. Kreuziger¹ · S. A. Young¹ · J. C. Heigel² · B. M. Lane² · T. Q. Phan²

Received: 27 September 2019 / Accepted: 13 February 2020 / Published online: 3 March 2020

© This is a U.S. government work and its text is not subject to copyright protection in the United States; however, its text may be subject to foreign copyright protection 2020

Abstract

Additive manufacturing (AM) of alloys creates segregated microstructures with significant differences from those of traditional wrought alloys. Understanding how the local build conditions generate specific microstructures is essential for developing post-build heat treatments with the goal of producing parts with reliable and predictable properties. This research examines the position- and orientation-dependent microstructures within IN625 Additive Manufacturing Benchmark Test specimens, including three-dimensional AM builds and individual laser traces on bare metal plates. Detailed characterizations of the solidification microstructures, compositional heterogeneities, grain structures and orientations, and melt pool geometries are described.

Keywords Additive manufacturing · Benchmarks · Model validation · AM-Bench · Microstructure

Introduction and Background

The extreme conditions that occur during a typical laser powder-bed fusion (LPBF) additive manufacturing (AM) build process (e.g., cooling rates on the order of 10^5 – 10^6 K/s and repeated heating/cooling cycles) can create components that exhibit high residual stresses, extreme compositional gradients, heterogeneous microstructures, and unexpected phases [1, 2]. As such, the degree of compositional heterogeneity in the as-built condition becomes highly dependent upon the local solidification conditions, which in turn, are strongly influenced by the size and shape of the melt pools created by the fundamental process parameters (scan speed, hatch spacing, scan path, laser power density, etc.) [3]. While the process parameters in LPBF have been the subject of recent research [4, 5], how those process parameters actually alter the as-built microstructure is not as well

characterized. This connection is important since the properties of any given alloy are determined by the microstructure which is highly dependent on the processing conditions [6–9]. Consequently, information that can be gained about the microstructure evolution, either through direct measurement or by validated numerical prediction, will better define the performance and/or reliability of an AM component in service [10].

Considering that direct measurement of all of the potential microstructural influences is impractical and expensive, the challenge becomes: can the AM community develop a set of accurate, validated numerical models that will be used consistently to predict the microstructure and/or performance of AM components? The National Institute of Standards and Technology (NIST) responded to this challenge by founding the Additive Manufacturing Benchmark Test Series (AM-Bench), with a goal of providing rigorous measurement data that modelers around the world can use to validate their AM models and codes. The first round of benchmark measurements for LPBF of metals have been completed (AM-Bench 2018) [3, 11–15], examining the relationships between process parameters, the local melt pool geometry and cooling rate, and the microstructure and phases within both individual laser melt tracks and solid parts. The single laser melt tracks were made using a combination of different laser power and speed settings on bare

✉ L. E. Levine
Lyle.Levine@nist.gov

¹ Materials Measurement Laboratory, National Institute of Standards and Technology, 100 Bureau Dr, Gaithersburg, MD 20899, USA

² Engineering Laboratory, National Institute of Standards and Technology, 100 Bureau Dr, Gaithersburg, MD 20899, USA

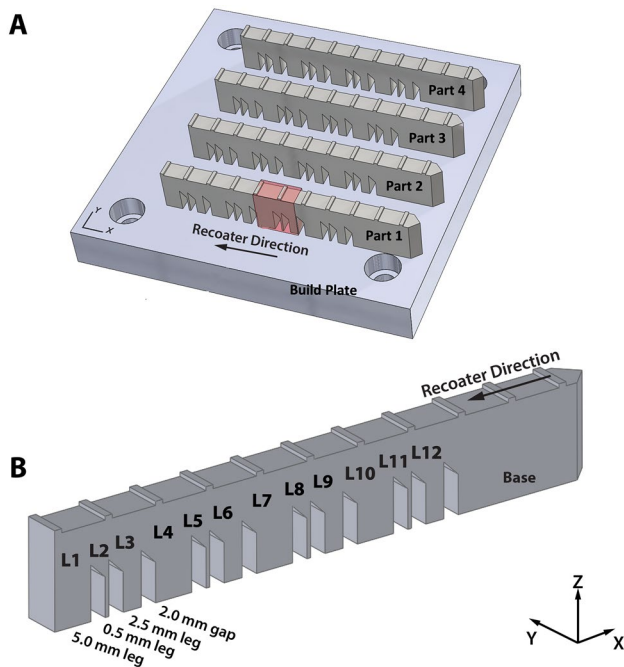


Fig. 1 Schematic drawings showing the artifacts used for the AM Benchmark tests. The arrangement of the artifacts on the build plate are shown in **a**, and the details of the thick and thin sections are shown in **b**

wrought plates of Inconel 625 (IN625), a nickel-based superalloy. Extensive in situ monitoring and post-build characterization of these melt tracks were carried out [3, 11]. For the three-dimensional (3D) AM builds, a simple part geometry (see Fig. 1) was additively built using LPBF with two well-characterized alloys: IN625 a nickel-based superalloy and SS15-5, a chromium–nickel-based, precipitation-hardenable martensitic stainless steel. The feedstock material of both alloys was extensively characterized including assessments of the powder composition, the powder size distribution, the powder production and conditioning methods, the atomization gas (e.g., nitrogen or argon), and the oxygen level during the build. Details pertaining to the powder composition and powder size distribution function can be found here: <https://www.nist.gov/ambench/amb2018-01-description>. Each build was highly controlled and accompanied by extensive in situ process monitoring [15].

The benchmark datasets for the 3D builds include detailed descriptions of the powder composition, powder size distribution, layer thickness, laser power, laser wavelength, laser power distribution at sample position, laser scan speed, and scan pattern with sub-millisecond-level timing (www.nist.gov/ambench/amb2018-01-description). Detailed in situ measurements of melt pool length and cooling rate were conducted for every layer through the highlighted region shown in Fig. 1a [15]. Thorough evaluations of the residual stresses [13], part distortion [13], and phases of the solidification

microstructure [12] were also included in each dataset [16]. Additional information about the scope of the benchmark tests can be found in the leadoff paper in this special issue [14] and on the AM-Bench website [17].

This paper presents results from the microstructure characterizations of the IN625 AM-Bench artifacts—specifically, the assessments of the melt pool geometries, microsegregation, and the solidification microstructure within the 3D builds and the individual melt tracks. Microstructure characterization of the 15-5 specimens will be reported separately.

IN625 was chosen because it is a well characterized, solid-solution strengthened, nickel-based superalloy that is commonly used for AM applications, largely due to the range of desirable properties (e.g., weldability, creep resistance, and corrosion resistance) [18]. The literature indicates that the pronounced segregation of solute elements during solidification increases the likelihood of precipitation of various secondary intermetallic phases such as δ -phase (DO_a Ni_3Nb), γ'' , Laves phases, and carbides that could influence the properties during service [19–26]. As such, IN625 is an ideal alloy system to examine the relationship between AM process parameters and the solidification microstructure.

It is important to note that the intent of this paper is to describe the measurement methods and measurement results of this microstructure characterization work. Detailed analyses and correlation with the other AM-Bench measurements will be published separately.

Materials, Methods, and Dataset Description

Coordinate System

In characterizing the microstructures of additively manufactured parts, different coordinate systems and sample directions may be relevant to the resulting microstructure, including the build plate coordinate system, the coordinate system of the specimen, the laser scan pattern, and the recoater blade direction. Here, all specimen orientations, including those for crystallographic texture analysis, will be described using the build plate coordinate system shown in Fig. 1. This coordinate system conforms to ISO/ASTM52921-13. The recoater blade motion is in the negative X direction as shown in Fig. 1b. The laser scan directions alternate between the X -axis for odd-numbered build layers and the Y -axis for even-numbered layers. Additional information on the scan strategy is given in [15].

Sample Identification

A schematic of the build plate used to make the benchmark artifacts is shown in Fig. 1a. Four identical artifacts were

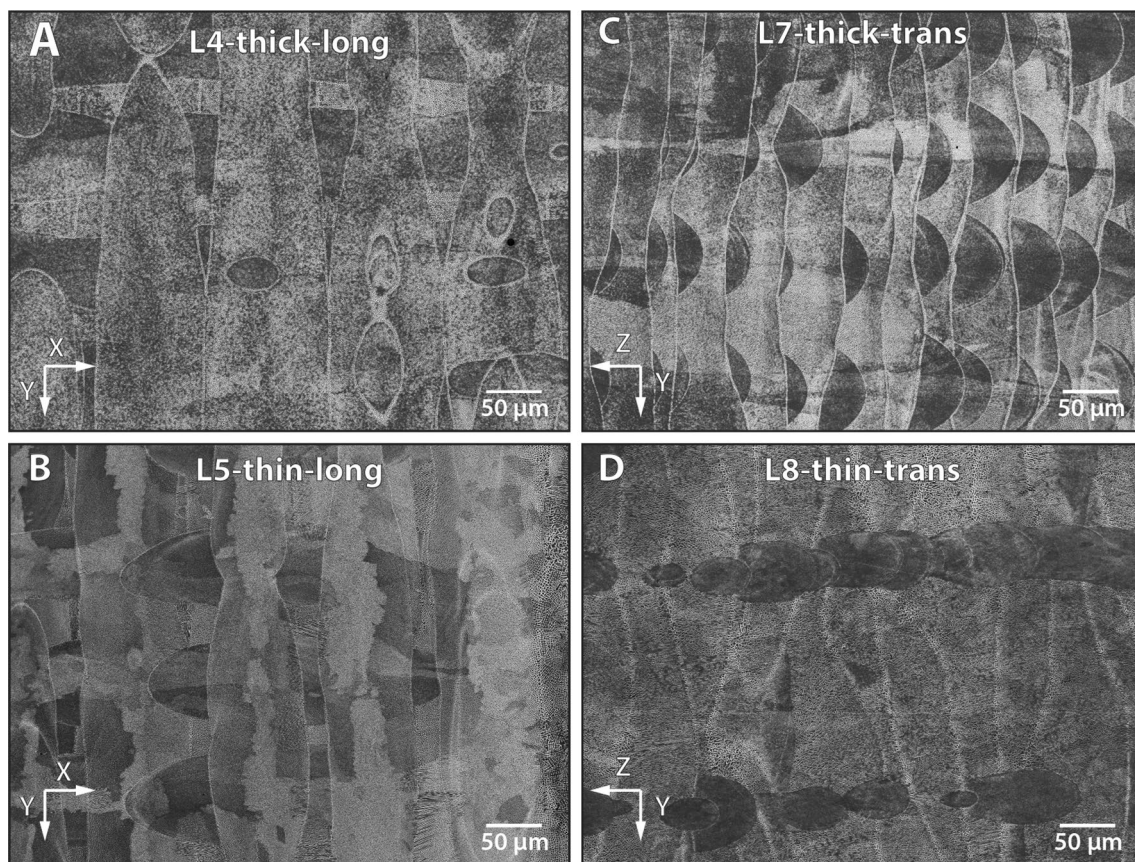


Fig. 2 Scanning electron micrographs showing the as-built microstructures of the benchmark artifacts. The thick and thin longitudinal sections (L4-thick-long, L5-thin-long) are shown in **a** and **b**, respec-

tively, and the thick and thin transverse sections (L7-thick-trans, L8-thin-trans) are shown in **c** and **d**, respectively, (aqua regia etch)

fabricated on each build plate and each was 75 mm long, 12 mm high, and 5 mm wide. The artifacts were spaced at 20 mm intervals along the *Y*-axis and were offset by 0.5 mm along the *X*-axis in order for the recoater blade to progressively engage each artifact. Parts were fabricated in the order they are labeled (i.e., Part 1 first, Part 4 last).

As shown in Fig. 1b, each specimen contains twelve ‘legs,’ where each leg is 7 mm in height including a 45° overhang below a solid bridge structure. Microstructure studies were conducted on ‘thick’ (5 mm nominal thickness) and ‘thin’ (0.5 mm nominal thickness) legs of the as-built specimens to evaluate the sensitivity of the microstructure evolution to the local geometry and specific solidification conditions in the build. Scanning electron microscopy (SEM) specimens were cut along the transverse (the *y*–*z* plane) and the longitudinal (the *X*–*Y* plane, or perpendicular to the base plate) orientations using wire electro-discharge machining (EDM).

Each specimen in this analysis had a unique identifier, which included the alloy designation, the LPBF machine used, the build plate number, part number, leg number, and sample orientation with respect to the build direction

(i.e., longitudinal or transverse). The complete designations for the individual samples were as follows: 625_CBM_B2_P1_L4 longitudinal (hereafter referred to as L4-thick-long), 625-CBM_B2_P1_L5 longitudinal (hereafter referred to as L5-thin-long), 625_CBM_B2_P1_L7 transverse (hereafter referred to as L7-thick-trans), and 625-CBM-B2_P1_L8 transverse (hereafter referred to as L8-thin-trans).

Melt Pool Characterization of 3D Builds

Specimens from each of the four legs were mounted in epoxy and polished according to standard metallographic procedure [27]. The melt pool structure was revealed by etching the specimens with aqua regia for approximately 30 s. The microstructures were examined in the SEM using both secondary electron (SEI) and backscattered (BSE) imaging techniques. A typical set of parameters used for the SEI analyses was a 5 keV accelerating voltage, a 1 nA probe current, and a 10 mm working distance. The depth of the electron interaction volume produced with 5 keV was small enough to limit the imaging to the near-surface structure,

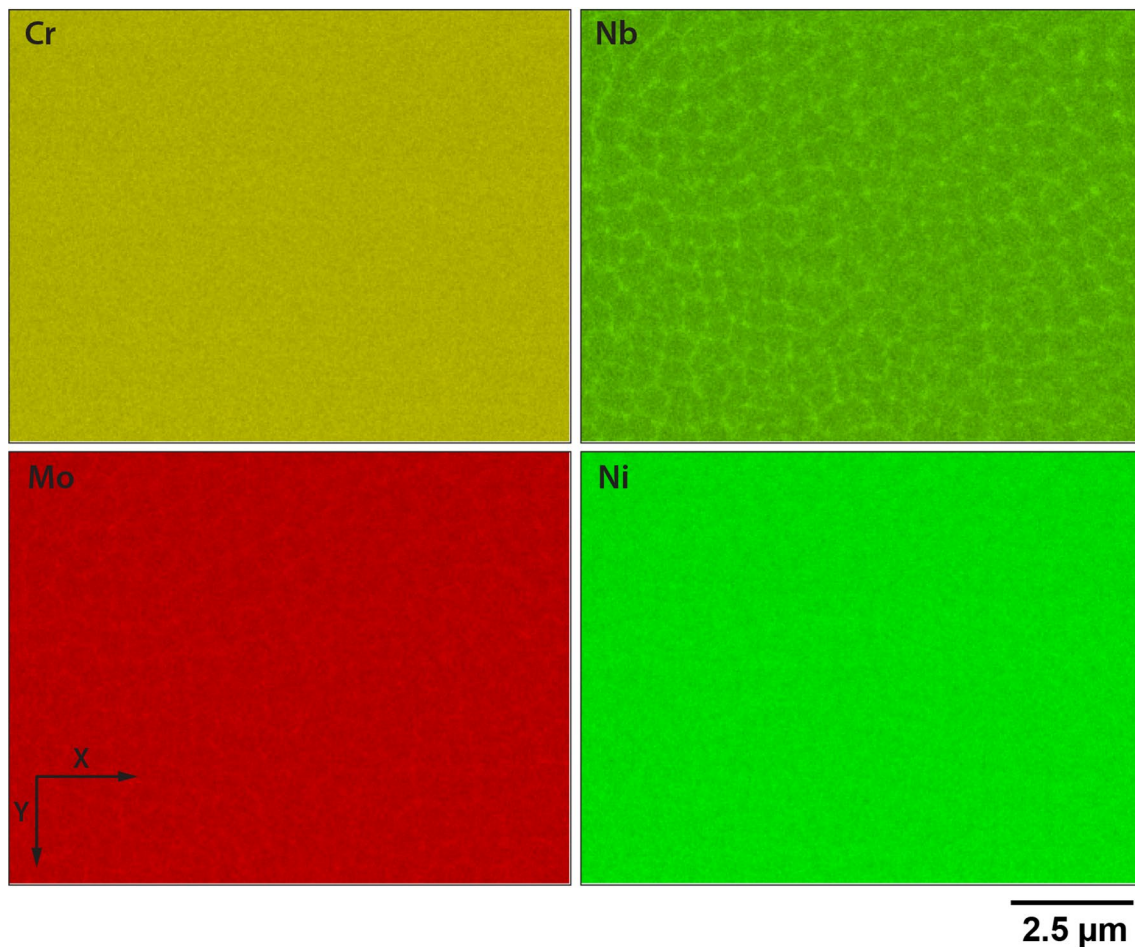


Fig. 3 EDS maps showing the composition variations produced by the local cooling conditions in the thick longitudinal section of the benchmark artifact (L4-thick-long)

which when combined with the 10 mm working distance, produced sufficient image contrast to clearly distinguish the macro-scale of the melt pool boundaries.

Examples of the etched as-built microstructures are presented in Fig. 2. Note that the axes shown in these figures indicate the orientation of the polished face with respect to the build plate coordinates. Figure 2a, b shows the melt pool structure for L4-thick-long and L5-thin-long, respectively. Similarly, Fig. 2c, d shows the melt pool structure for L7-thick-trans and L8-thin-trans, respectively. High-resolution images from the melt pool characterization are available in the AM Bench data archive: <https://www.nist.gov/ambench/chal-amb2018-01-mspfpfrs>. The strong spatial variation in the primary arm spacing visible in these images is indicative of significant local variation in the cooling conditions and could serve as a useful target for model validation.

Microsegregation Analysis of 3D Builds

The etched samples were re-polished and prepared for compositional analysis with vibratory polishing in a colloidal SiC suspension for a minimum of 8 h. This step removed any remaining deformation that could have been introduced during the mechanical polishing and produced a strain-free surface that was suitable for high-resolution analyses of the microsegregation in the SEM. The degree of elemental segregation in each of the four specimens was assessed with X-ray energy dispersion spectroscopy (EDS). The imaging parameters for these analyses (i.e., 15 keV accelerating voltage, 0.5 nA probe current, and 10 mm working distance) produced a deadtime on the order of 10%. Previous analyses revealed that the composition varies over length scales of 10 s of nm [24, 28, 29]. At these length scales, quantitative EDS analyses do not yield accurate results due to the electron beam interaction volume greatly exceeding the feature size. For this reason, the EDS analyses performed on

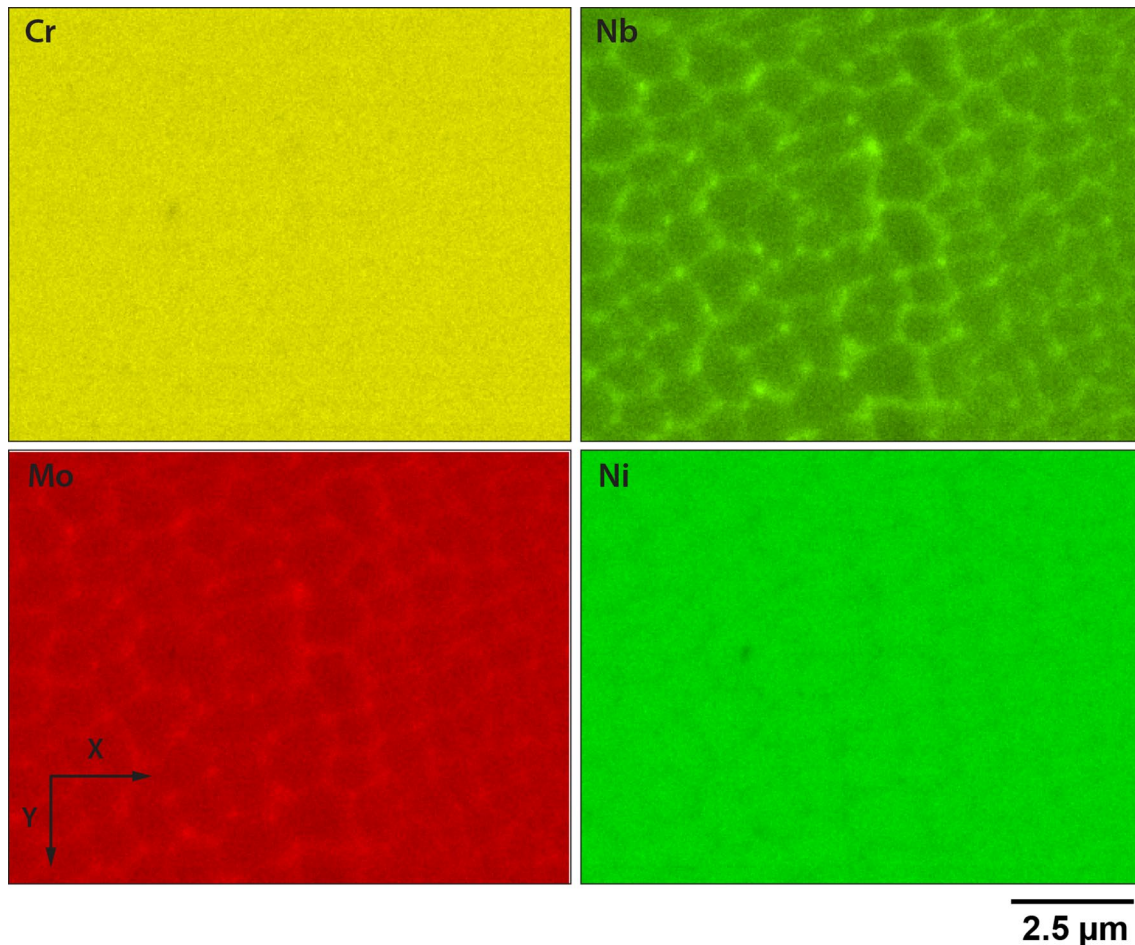


Fig. 4 EDS maps showing the composition variations produced by the local cooling conditions in the thin longitudinal section of the benchmark artifact (L5-thin-long)

the benchmark artifacts could only be used for a qualitative comparison.

The results from the EDS analyses on the four as-built specimens are presented in Figs. 3 through 6. The orientations of the four specimens are identical to those shown in Fig. 2. Since microsegregation in IN625 promotes the precipitation of Nb-rich intermetallic secondary phases (e.g., δ -phase, and γ'') during post-build annealing, the maps presented in these figures have been limited to the set of elements most likely to promote those phases, namely Nb, Mo, Cr, and Ni. In the as-built condition examined here, no secondary phases were detected using either SEM or synchrotron X-ray powder diffraction [12].

Figures 3 and 4 are EDS maps of L4-thick-long and L5-thin-long, respectively. In situ cooling rate measurements during the builds showed that the thick legs exhibited a slower cooling rate overall than the thin legs, with larger variations between even and odd build layers [15]. Similarly, Figs. 5 and 6 are EDS maps of L7-thick-trans and

L8-thin-trans, respectively. Additional EDS elemental maps are available in the data archive.

Crystal Orientation Analysis of 3D Builds Using Spatially Resolved Maps

The solidification microstructure in each of the four specimens was also examined using electron backscatter diffraction (EBSD). This study focused on the grain size distribution, orientation, and texture. The imaging conditions used for the EBSD were similar to those used for the melt pool and microsegregation analyses, the key differences being a higher accelerating voltage of 20 keV was used along with a significantly higher beam current (approximately 10 nA). A higher current optimized the signal to resolve the electron backscatter patterns (EBSP) and minimize the acquisition time. In addition, all of the

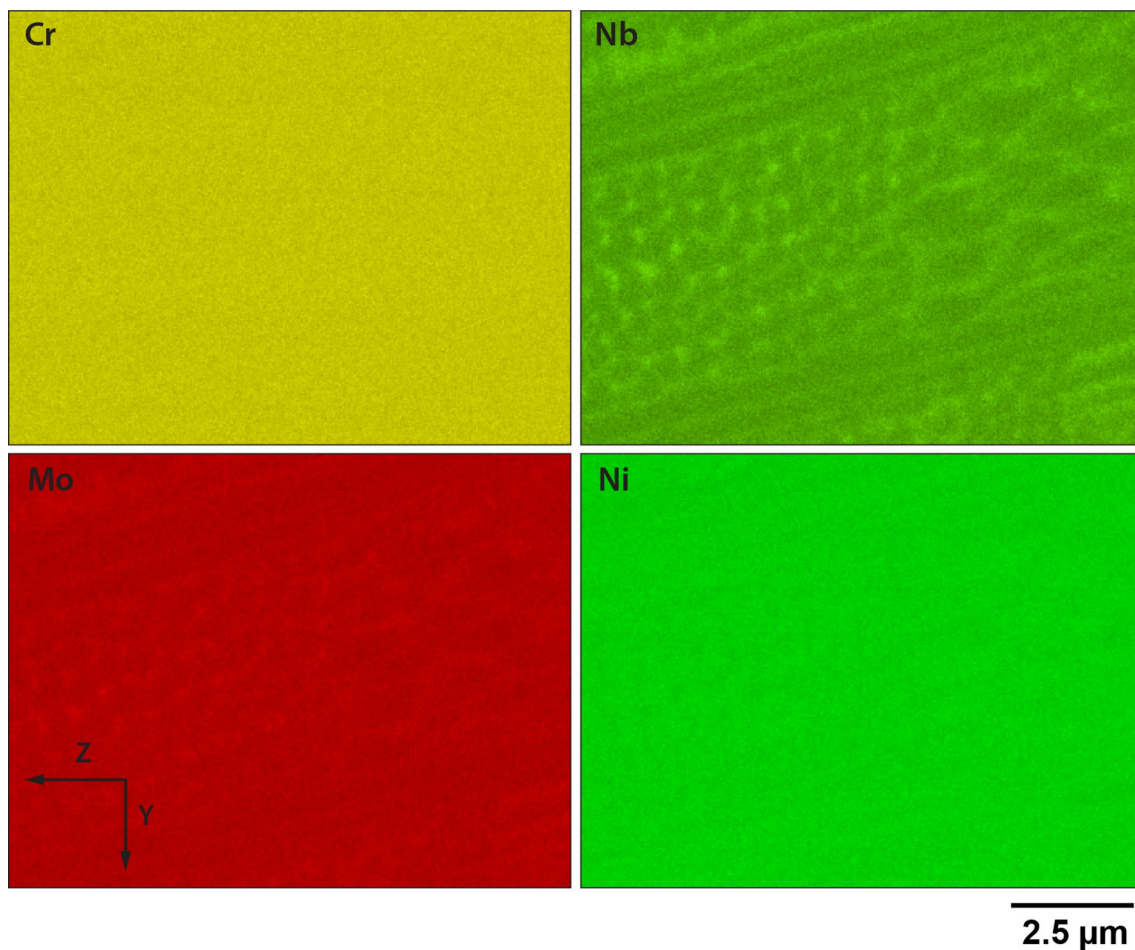


Fig. 5 EDS maps showing the composition variations produced by the local cooling conditions in the thick transverse section of the benchmark artifact (L7-thick-trans)

EBSD data were acquired with 1×1 binning, an inter-pixel spacing of $1.4 \mu\text{m}$, and no pixel averaging. Although the microstructure generated by the 0° – 90° laser scan pattern was reasonably periodic on the macro-scale, substantial micro-scale variations were observed depending on the location. As such, the EBSD maps were acquired systematically from a matrix of adjacent sites at a magnification that captured both the large- and small-scaled variations. Large-area maps, approximately $1.4 \text{ mm} \times 1.0 \text{ mm}$, were constructed from the individual maps with image stitching software. After the large-area maps were assembled, they were analyzed and plotted using the software package *mtex* [30].¹

¹ Certain commercial entities, equipment, or materials may be identified in this document to describe an experimental procedure or concept adequately. Such identification is not intended to imply recommendation or endorsement by the National Institute of Standards and Technology, nor is it intended to imply that the entities, materials, or equipment are necessarily the best available for the purpose.

Spatially resolved orientation maps for the four as-built specimens are presented in Fig. 7 through 10. Figures 7 and 8 are orientation maps in the X, Y, and Z sample directions for the two different leg thicknesses in the longitudinal orientation (i.e., the X–Y plane). Similarly, Figs. 9 and 10 are orientation maps for the two different leg thicknesses in the transverse orientation (i.e., the Y–Z plane). The sample orientations in the build coordinate system are shown in each figure. The inverse pole figure (IPF) indicates the crystal orientation at each pixel relative to the build plate sample axes X, Y, and Z colored according to the IPF key. For example, red pixels indicating the [001] direction of the crystal is parallel to the assigned sample direction, green pixels indicating the [101] direction of the crystal is parallel to the assigned sample direction, and blue pixels indicating the [111] direction of the crystal is parallel to the assigned sample direction. In these figures, adjacent pixels with a 2° misorientation angle are delineated by a thin line, and those with an angle of 10° or higher are delineated by heavier lines. All samples other than the L5-thin-long used a 3×3 matrix of

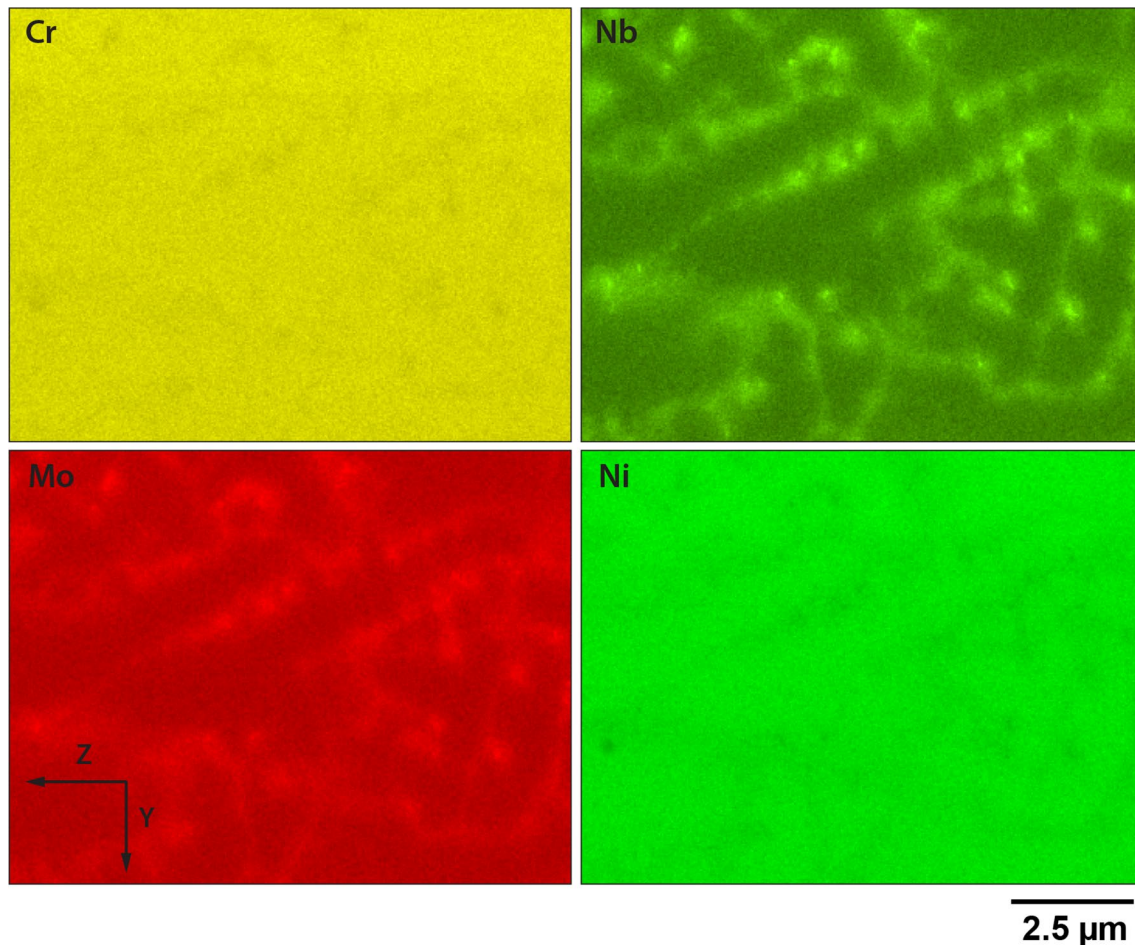


Fig. 6 EDS maps showing the composition variations produced by the local cooling conditions in the thin transverse section of the benchmark artifact (L8-thin-trans)

scan sites and a region size described above. Due to the sample shape, the maps shown for the L5-thin-long sample in Fig. 8 were constructed from a 1×8 matrix, which enclosed a region approximately $0.450 \text{ mm} \times 2.6 \text{ mm}$. Note that these figures were constructed from raw data, i.e., no post-analysis filling of unindexed pixels. However, the unindexed pixels were not included in the grain boundary calculations.

Crystal Orientation Analysis of 3D Builds Using Pole Figures

While inspection of the spatially resolved data can give some indication if there are preferred grain orientations or crystallographic texture in the microstructure, an alternative representation is a series of pole figures. A material is considered to have a random (or uniform) texture if the crystal orientations in a given sample are distributed evenly across a pole figure. It is important to note that pole figures do not explicitly indicate the complete orientations of the crystals

in a polycrystalline sample; they only indicate the orientations of selected crystalline planes [31].

Groupings of particular orientations on a pole figure can indicate texture, and some orientations have shorthand names such as ‘cube,’ ‘Goss,’ ‘shear,’ etc., that are widely used in the literature. However, many of these shorthand names have their origins in rolled sheet products, which have a rolling direction (RD), transverse direction (TD), and normal direction (ND) sample axes convention. As mentioned previously, for additive manufacturing products, a variety of coordinate systems and directions are relevant. Orientations in this paper are defined with reference to the build plate coordinate system that follows ISO/ASTM specifications. Table 1 lists the definitions of the texture shorthand notations that are used in this paper.

Upper hemisphere pole figures showing the average grain orientations from the four samples are shown in Fig. 11. The (100), (110), and (111) pole figures are shown for the L4-thick-long, L5-thin-long, L7-thick-trans, and L8-thin-trans samples in Fig. 11a–d, respectively. The sizes of the

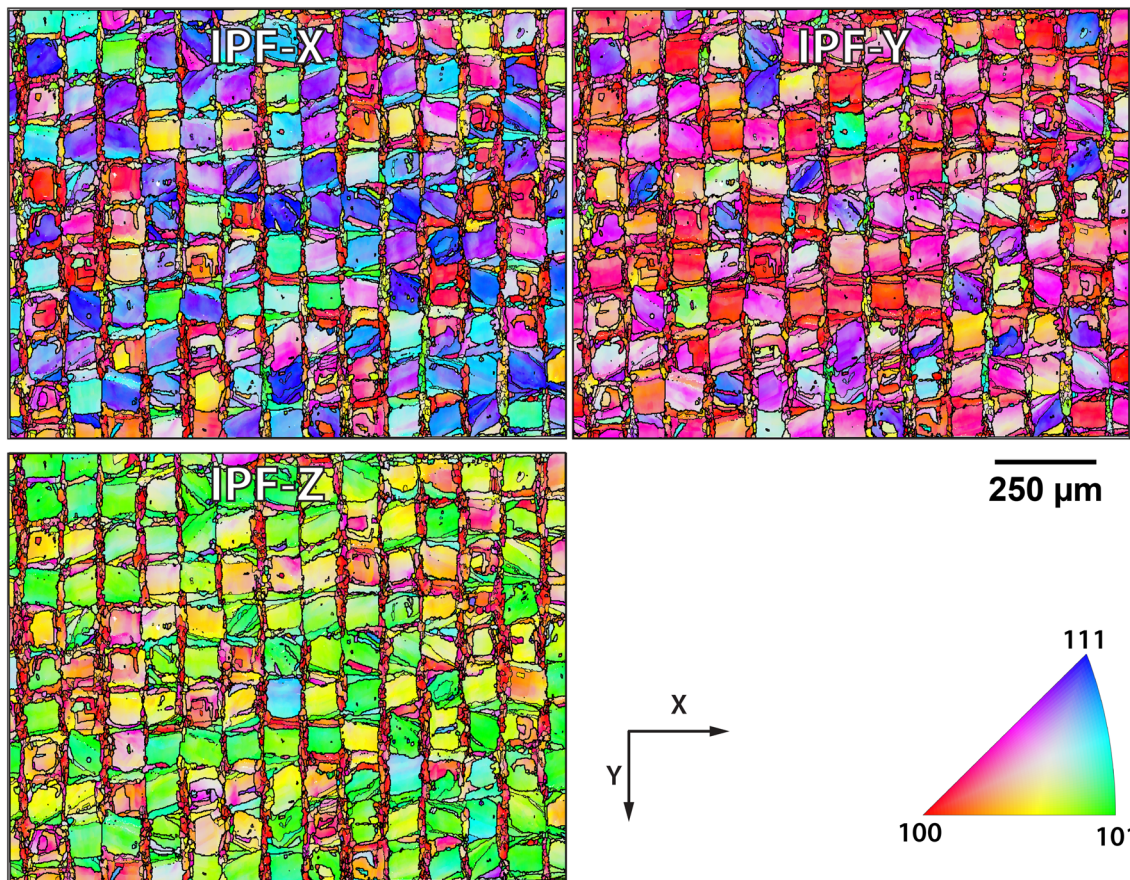


Fig. 7 EBSD inverse pole figure maps showing the orientations in the solidification microstructure with respect to the build plate axes of the thick longitudinal section of the benchmark artifact (L4-thick-long)

‘dots’ shown in Fig. 11a–c are proportional to the square root of the grain area, such that a larger dot represents a larger grain with a particular orientation. As shown in Fig. 10, the average grain size of the L8-thin-trans specimen was substantially smaller than the others, which produced an extremely high density of points in the pole figure. This type of scaling was impractical for this pole figure, so Fig. 11d shows a subset of the data to better illustrate the trends. Since no mechanical processing was performed on these samples, any texture developed likely occurred during solidification as a function of location in the part, scan strategy and build orientation.

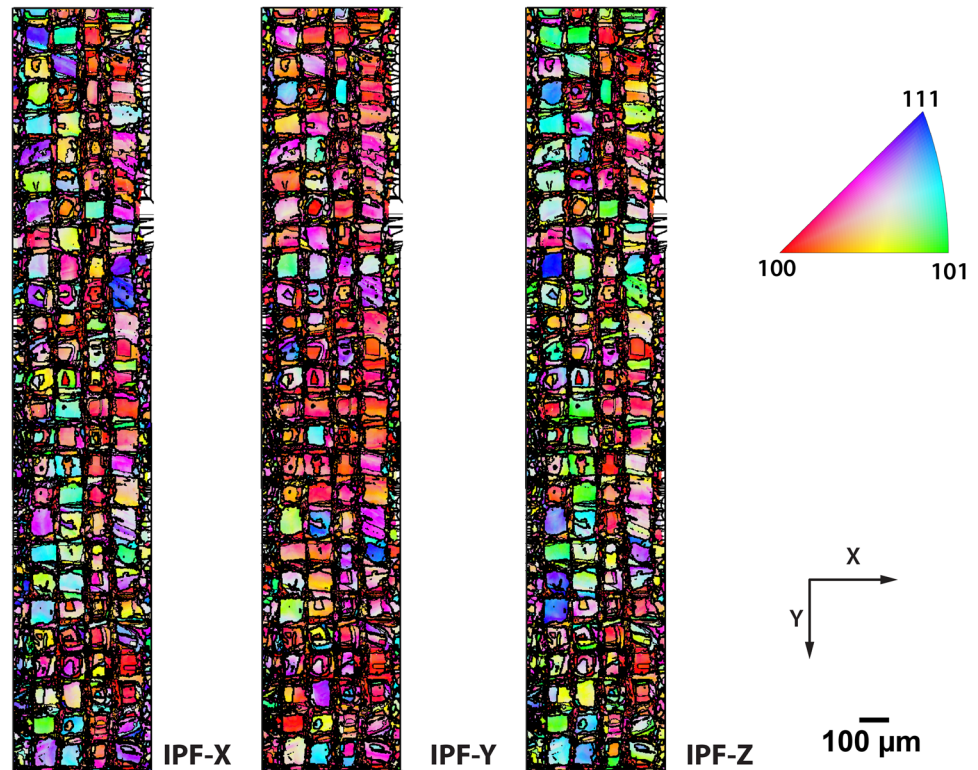
Solidification Microstructure of Individual Laser Tracks

An additional set of measurements was conducted on individual laser scan tracks that were made on the surface of a bare, IN625 plate, measuring approximately 24 mm by 25 mm, and 3.2 mm thick. The as-received plates were likely hot-rolled as no evidence of deformation from rolling was

observed in the plate microstructure. No additional heat treatments were performed, but the plate surface was polished using standard metallurgical procedures to a moderate pressure, randomly oriented 320-grit finish. Three different laser power and speed combinations were used, and multiple replications of each power/speed setting were made for each combination. In situ measurements of the melt pool length and the cooling rate of the solidified material were performed on each trace [11], and the 3D surface topography of the melt traces was measured using confocal scanning laser microscopy [3].

The laser tracks were produced using the NIST Additive Manufacturing Metrology Testbed which is instrumented for in situ thermographic measurements. The tracks were produced using three different power/speed combinations: Case A, 137.9 W and 400 mm/s; Case B, 179.2 W and 800 mm/s; Case C, 179.2 W and 1200 mm/s. The measured laser power distribution function was Gaussian with a diameter (given by $D4\sigma$, i.e., 4 times the Gaussian standard deviation) of 170 μm , and the full width at half-maximum (FWHM) was 100 μm . The in situ measurement results and a complete

Fig. 8 EBSD inverse pole figure maps showing the orientations in the solidification microstructure with respect to the build plate axes of the thin longitudinal section of the benchmark artifact (L5-thin-long)



description of the measurement methods are presented in Ref. [11].

After topographical characterization in the confocal microscope [3], the plate with the laser traces was cross-sectioned and mounted to examine the microstructure in the autogenous weld zones. A second piece of the plate was mounted directly adjacent to the region of interest to prevent rounding of the weld nugget during mechanical polishing. Even though the two pieces were in contact macroscopically, small gaps between the two pieces were noticeable, which were mostly filled with epoxy during the mounting process. A ‘marker lithography’ process was used to prevent charging in the SEM by the non-conductive epoxy. Upon completion of the final polishing step, thin lines were drawn over the regions of interest with a magic marker to create a mask, and then the entire sample was sputter-coated with a thin layer of gold. The sample was then rinsed with alcohol to dissolve the marker, leaving the gold coating in the epoxy regions. The solidification microstructure was revealed by etching the specimen with aqua regia for approximately 30 s. The cross sections were examined in the SEM using both SEI and BSE techniques. Upon completion, the etched surface was carefully removed using a vibratory polisher for EBSD analysis. Care was used to ensure that minimal material was removed during this process so that the grain structure visible in the EBSD maps corresponds to the grain-dependent solidification microstructure visible on the etched surfaces.

Figure 12 presents both the etched microstructure and the series of orientation maps in IPF coloring for the three power/speed combinations. Each image of the etched solidification microstructure is a mosaic consisting of multiple high-resolution images that were taken at specific locations stepped across the entire area of the autogenous weld zone. These images clearly demonstrate that the solidification front in the weld zone initiated epitaxially with the structure of the parent metal. High-resolution images of the solidification microstructure can be found on the website: <https://www.nist.gov/ambench/chal-amb2018-02-dmgs>. Since multiple tracks were made on each specimen, the images on the website are indexed by the individual laser track number. That is, track 3 (179.2 W, 1200 m/s) corresponds to Case C, track 5 (137.9 W, 400 m/s) to Case A, and track 10 (179.2 W, 800 m/s) to Case B.

Crystal Orientation Analysis of Individual Laser Tracks

The orientation maps shown in Fig. 12 were constructed with the same parameters used for the maps constructed from the 3D specimens, (i.e., adjacent pixels with a 2° misorientation angle are delineated by a thin line, and those with an angle of 10° or higher are delineated by heavier lines), and as was the case in the analysis of the 3D builds, a full analysis of the grain distributions, including the Euler angles from each grid point, is available in the online AM-Bench data:

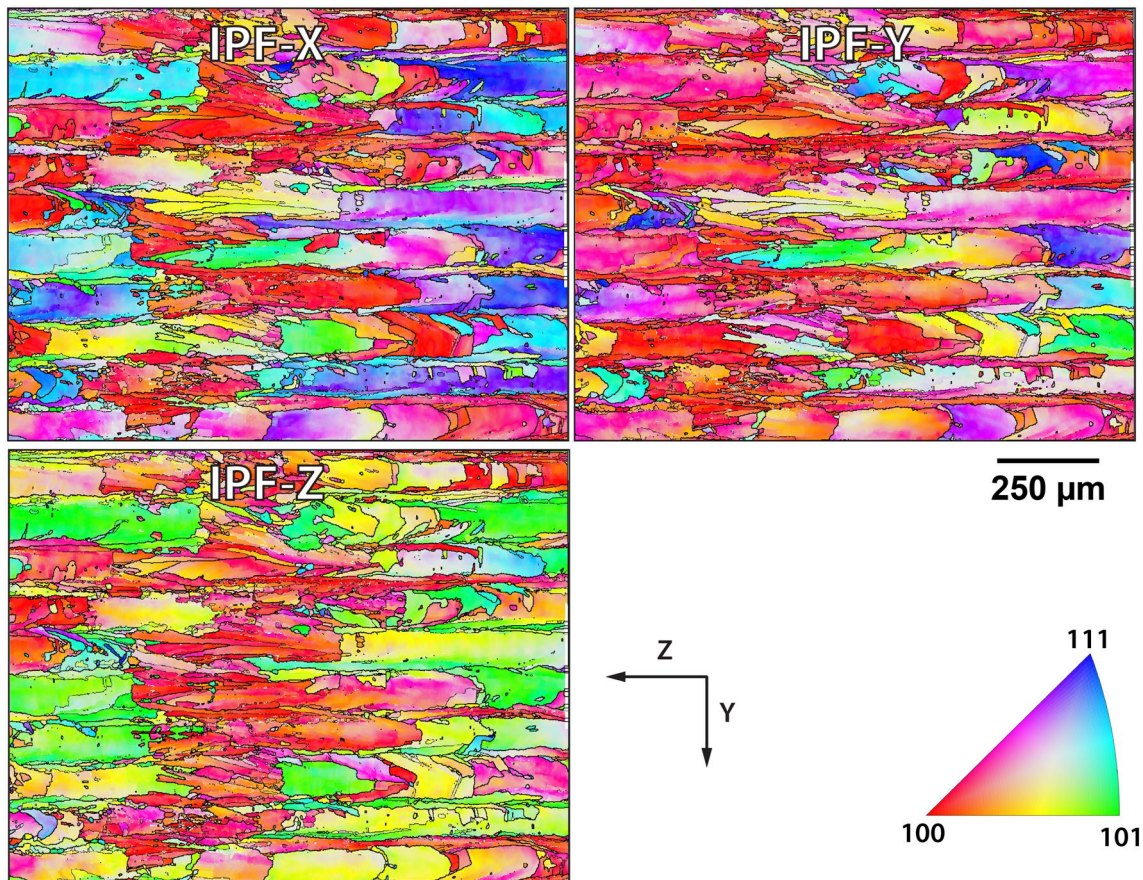


Fig. 9 EBSD inverse pole figure maps showing the orientations in the solidification microstructure with respect to the build plate axes of the thick transverse section of the benchmark artifact (L7-thick-trans)

<https://www.nist.gov/ambench/chal-amb2018-01-mspfpfrs>. Recalling that the inverse pole figure (IPF) coloring in these maps indicates the orientation at each pixel according to the triangle shown, and that the coloring in an IPF map will be different depending on which crystal direction is parallel to the sample direction that defines the IPF, orientation maps with respect to the X , Y , and Z directions are included for each trace in the figure. Considering that the microstructure of the substrates consisted entirely of equiaxed grains, and that the solidification front was primarily epitaxial with the substrate microstructure, it is not surprising that no apparent preferred crystal orientation is observable in the weld zones.

Example Analysis and Discussion of the Dataset

The key factor for the AM-Bench measurements is the providence of the raw materials, artifact fabrication methods, sample preparation methods, and the in situ and ex situ data. The metrology of all the primary factors that affect the

structural integrity of an AM component, e.g., the assessment of the laser parameters, and the in situ layer-by-layer, time resolved local measurements of melt pool length, and cooling conditions, created a unique dataset [3, 11]. In addition, each component in this dataset was designed to maximize the fidelity between a model-based prediction and the physical measurement. These data are provided to the AM community to use as benchmarks in their analysis. Some analyses by the authors are included below as examples of what can be explored in this dataset.

EDS Data

The data from the EDS analyses suggest the segregation that occurred during the build process is similar to that observed in other studies [23, 25]. The EDS maps in Figs. 3 through 6 and the solidification microstructures shown in Figs. 2 and 12 indicate that the rapid cooling process in LPBF promotes segregation of Nb and Mo to the inter-dendritic regions in the IN625. Consequently, the dendrite cores tend to be enriched in Ni and Cr [22, 25]. As noted earlier, the size scale of the inter-dendritic regions is smaller than the

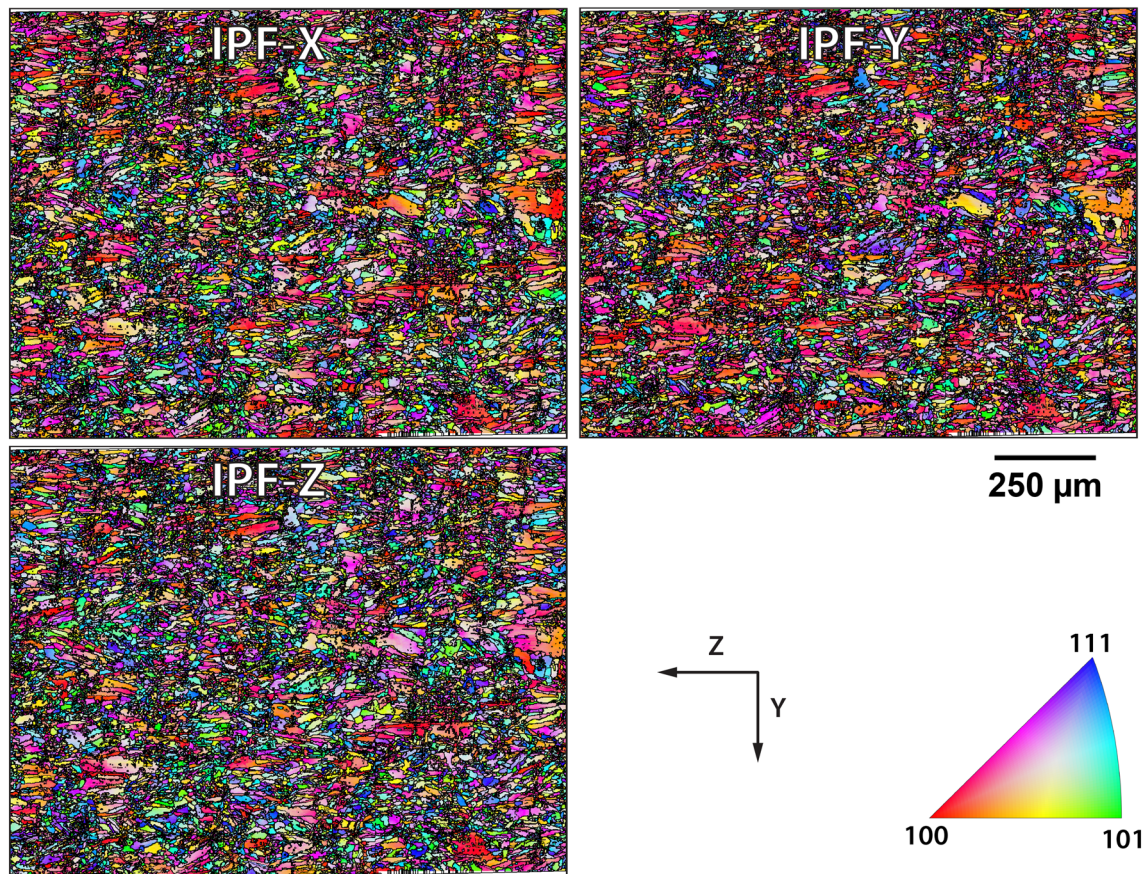


Fig. 10 EBSD inverse pole figure maps showing the orientations in the solidification microstructure with respect to the build plate axes of the thin transverse section of the benchmark artifact (L8-thin-trans)

Table 1 Crystal orientations and IPF coloring for each sample axis

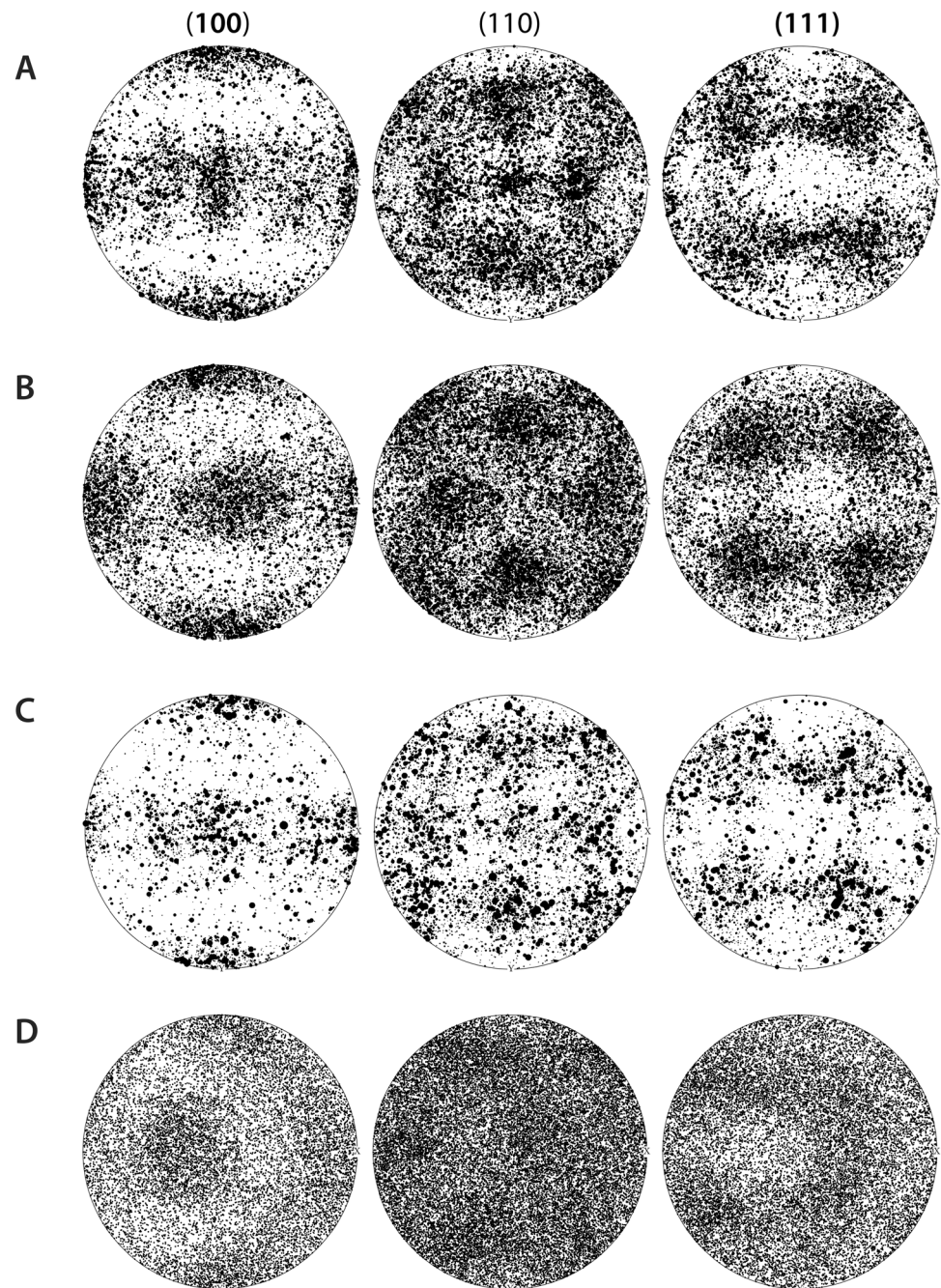
Shorthand name	Plane (Z-axis)	Direction (X-axis)	X-axis color	Y-axis color	Z-axis color
Cube	{001}	$\langle 100 \rangle$	Red	Red	Red
Shear	{001}	$\langle 1\bar{1}0 \rangle$	Green	Green	Red
Goss	{011}	$\langle 100 \rangle$	Red	Green	Green
Rotated Goss	{011}	$\langle 01\bar{1} \rangle$	Green	Red	Green

EDS sampling volume, making it impossible to obtain a reliable and quantitative determination of the segregation distribution function. Also, higher magnification images of the solidification microstructures shown in Fig. 2 (available in the AM-Bench 2018 data archive) exhibit the same grain–grain variations visible in the single laser trace cross sections in Fig. 12. Thus, the variations in the size scale of the local cellular structures in the EDS maps are likely caused by differences in the local cooling conditions, or to differences in the local microstructure at the point where the data were acquired. However, the morphology of the segregation acquired in the longitudinal plane is substantially different from that in the transverse plane. Additional data showing differences in the segregation between the thick and

thin legs were obtained using synchrotron X-ray diffraction measurements [12]. The magnitude of this segregation for as-built LPBF IN625 produced using a different scan strategy has also been discussed previously [28].

As mentioned above, combining information from the laser and laser scan parameters, the in situ thermographic measurements (providing local cooling rate), the large-area solidification microstructure images, and the segregation data from the EDS maps, one should be able to validate detailed model predictions for the local dendrite composition and morphology. Models of this type are necessary to develop optimized post-build heat treatments for residual stress relief, homogenization, recrystallization, precipitation, etc.

Fig. 11 EBSD upper hemisphere pole figures showing the average grain orientations from the thick and thin longitudinal sections (**a** and **b**, respectively), and the thick and thin transverse sections (**c** and **d**, respectively)



EBSD Data: Grain Shape

The spatially resolved EBSD maps revealed that both longitudinal sections (L4-thick-long in Fig. 7 and L5-thin-long in Fig. 8) exhibit square regions with large grains (approximately $100\ \mu\text{m} \times 100\ \mu\text{m}$) that are delineated by smaller grains that have elongated aspect ratios parallel to the X and Y axes. This structure is likely caused by the square raster pattern of the laser during the build process. Recent AM work on the single phase CoCrFeMnNi face centered cubic system suggests that the small grains may mark the centers

of the solidified melt pools, rather than the edges [32], but additional data are required to make a determination for this case. The highly elongated grain structure shown in Fig. 9 reflects the large square grains in Fig. 7 seen in cross section, demonstrating substantial epitaxial growth in the build direction (Z axis) as the typical grain lengths of $250\text{--}600\ \mu\text{m}$ are substantially longer than the $20\ \mu\text{m}$ layer thickness of the 3D build. Note that the ‘small’ grains in Fig. 7 with small Y -axis dimensions also extend long distances along the build direction, as shown in Fig. 9. In contrast, the extremely fine grain structure in Fig. 10 likely corresponds to a transverse

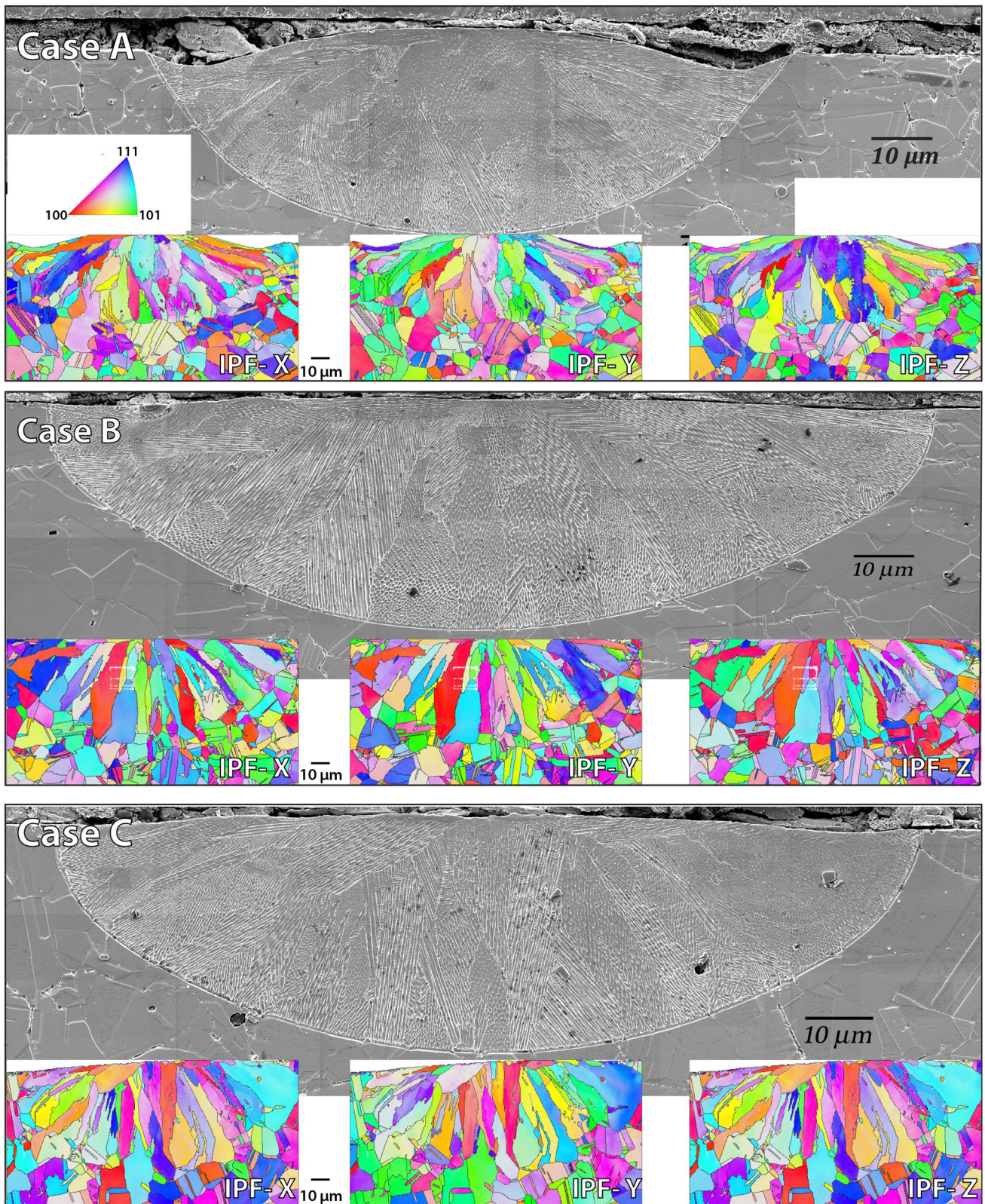


Fig. 12 Etched microstructures and corresponding series of orientation maps in IPF coloring for the cross sections of three single laser tracks with different power/speed combinations

slice through the small-grain regions between the large square grains in Fig. 8 (L5-thin-long). While some of these grains are extended along the build direction, it is much less than observed in Fig. 9.

EBSD Data: Crystal Orientation

For an example analysis of the EBSD data, the IPF-Z map for L4-thick-long (Fig. 7) shows that the crystal orientations of the larger grains have a preferred orientation with the crystal [110] axis parallel to the Z-axis (build direction). This can also be seen in the (110) pole figure maps for this sample (Fig. 11a) as a concentration of points in the center (parallel to X-axis) of the plot. However, the IPF Z map of the transverse L7-thick-trans sample in Fig. 9 does not show this same concentration of points in the (110) pole figure (Fig. 11c). Examining the spatially resolved EBSD data in Fig. 9 along the Z-axis, there appear to be extended regions where the grains exhibit different dominant crystal orientations, alternating between bands where the [100] or the [110] are parallel to the Z-axis (build direction). This pattern does not seem correlated to the even or odd layer size, as the orientations are roughly consistent over a particular grain, which extend approximately 500 μm in the Z axis. Thus, the apparent texture described above for Fig. 10 may not hold throughout the build but may vary or alternate along the Z axis. The different cross section views provide complimentary grain shape and orientation data that can facilitate comparison with grain growth models and be used to check if the cross section is representative of the whole microstructure. The measured textures and grain sizes can provide a valuable test for microstructure evolution models that attempt to incorporate local cooling rate effects that result from the laser power, speed, power distribution function, and scan pattern.

EBSD Data: Crystal Size and Orientation

Qualitative inspection of the IPF maps for L4-thick-long (Fig. 7) indicates that there may be different textures between the larger square-shaped grains and the smaller and higher aspect ratio grains between the larger grains, as evidenced by the predominance of large grains in the IPF-Z map to be oriented near the [101] axis (green), and the smaller grains to be oriented near the [100] axis (red). To investigate this further, the EBSD data were partitioned into ‘large’ and ‘not large’ grains, with a threshold of 1500 μm^2 in grain area. Pole figures can then be extracted from the partitioned grains and compared. These data are shown in Fig. 13. Figure 13a repeats the IPF-Z map shown in Fig. 7. Figure 13b depicts all the grains that are in the ‘large’ subset. Figure 13c, d

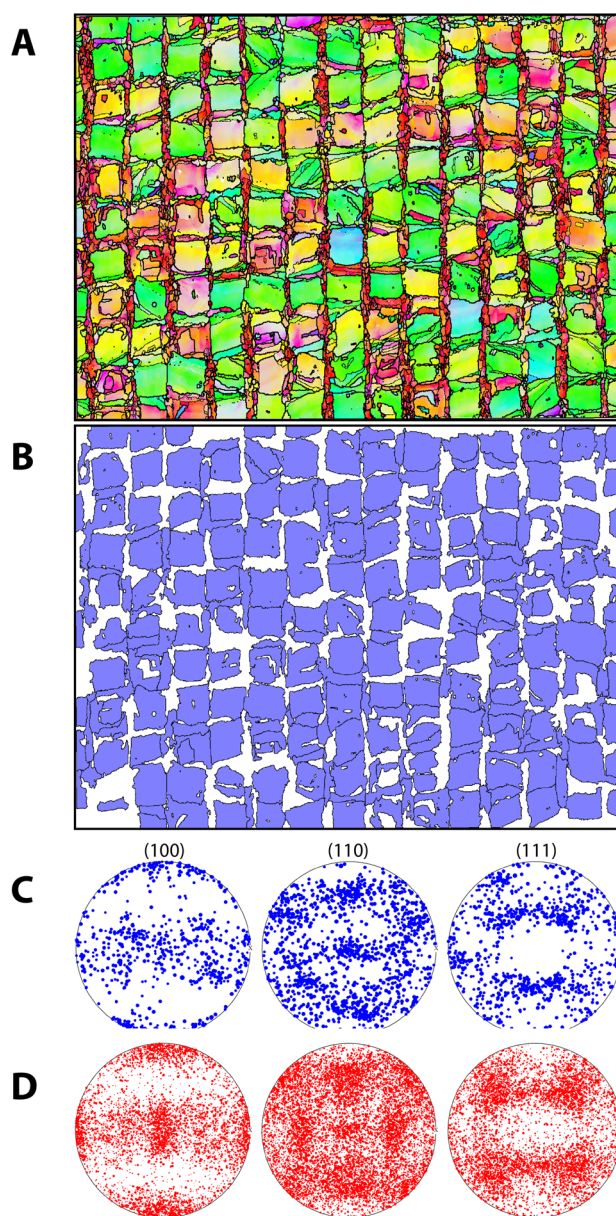


Fig. 13 Subset of inverse pole figure Z map from Fig. 7 showing grains with areas larger than 1500 μm^2 (Fig. 12b). The corresponding pole figure for the subset with grain areas larger than 1500 μm^2 is shown in Fig. 12c, and the subset for the grains with areas less than 1500 μm^2 is shown in Fig. 12d

is the pole figures for the ‘large’ and ‘not large’ subsets, respectively.

While there is a limited number of grains in these subsets (220 in ‘large’ and 2107 in ‘not large’) some trends are noticeable. The ‘not large’ grains are closer to a cube texture, with a clear clustering of grains with [100] axis parallel to the Z-axis. In contrast, the ‘large’ grains have

a nearly even distribution of [100] grain axes along the X–Z axis. However, in both datasets there is a cluster of grains with a [110] axis close to the Z-axis, indicative of a different texture such as Goss or rotated Goss. Also, the clustering or absence of grains of a specific orientation is rather similar within both datasets. Therefore, the qualitative inspection of a different texture is not completely borne out in additional analysis. This type of analysis can serve as a check when investigating if there are statistically significant differences between the two grain sizes.

Summary

A dataset comprising melt pool characterization, microsegregation analysis, and crystal orientation has been summarized for two structural elements (legs) from an AM Benchmark ‘bridge’ artifact that was additively built from a nickel-based superalloy (IN625). The elements were classified by the relative thickness (thick or thin) and by the orientation with respect to the build axis (longitudinal or transverse). This enabled an evaluation of the microstructure for two different local solidification conditions in orthogonal orientations. The dataset also includes characterizations of solidification microstructures within cross sections of single laser traces on an IN625 substrate, obtained using three different laser power and speed settings.

Individually, these assessments of the melt pool geometries, the microsegregation, and the solidification microstructure within the 3D builds and the individual melt tracks were intended to complement a broader set of rigorous, validated, additive manufacturing test data designed to provide modelers with a basis to gauge the accuracy of their numerical simulations. Each assessment was designed to be complete so that the data can be used for a specific simulation or in conjunction with a larger model. When viewed collectively, this set of assessments characterizes the complexity of the microstructures created in an AM build process.

Acknowledgements Part of this research was supported by the Exascale Computing Project (17-SC-20-SC), a collaborative effort of the U.S. Department of Energy Office of Science and the National Nuclear Security Administration.

Compliance with Ethical Standards

Conflict of interest On behalf of all authors, the corresponding author states that there is no conflict of interest.

References

- Dey GK, Albert S, Srivastava D, Sundararaman M, Mukhopadhyay P (1989) Microstructural studies on rapidly solidified Inconel 625. *Mater Sci Eng A* 119:175–184
- Dinda GP, Dasgupta AK, Mazumder J (2009) Laser aided direct metal deposition of Inconel 625 superalloy: microstructural evolution and thermal stability. *Mater Sci Eng A* 509:98–104
- Ricker RE, Heigel JC, Lane BM, Zhirnov I, Levine LE (2019) Topographic measurement of individual laser tracks in alloy 625 bare plates. *Integr Mater Manuf Innov* 8(4):521–536
- Liverani E, Toschi S, Ceschini L, Fortunato A (2017) Effect of selective laser melting (SLM) process parameters on microstructure and mechanical properties of 316L austenitic stainless steel. *J Mater Proc Technol* 249:255–263
- Brown CU, Jacob G, Possolo A, Beauchamp CR, Peltz MA, Stoudt MR, Donmez AM (2018) NIST advanced manufacturing series 100–19. NIST, Gaithersburg. <https://doi.org/10.6028/NIST.AMS.100-19>
- Olson GB (1997) Computational design of hierarchically structured materials. *Science* 277:1237–1242
- Beaudoin AJ, Acharya A, Chen SR, Korzekwa DA, Stout MG (2000) Consideration of grain-size effect and kinetics in the plastic deformation of metal polycrystals. *Acta Mater* 48:3409–3423
- Thornton K, Nola S, Garcia RE, Asta M, Olson GB (2009) Computation in the materials science and engineering core. *JOM* 61:12–17
- Xiong W, Olson GB (2015) Integrated computational materials design for high-performance alloys. *MRS Bull* 40:1035–1044
- Roters F, Eisenlohr P, Hantcherli L, Tjahjanto DD, Bieler TR, Raabe D (2010) Overview of constitutive laws, kinematics, homogenization and multiscale methods in crystal plasticity finite-element modeling: theory, experiments, applications. *Acta Mater* 58:1152–1211
- Lane BM, Heigel JC, Ricker R, Zhirnov I, Khromschenko V, Weaver J, Phan TQ, Stoudt MR, Mekhontsev S, Levine LE (2020) Measurements of melt pool geometry and cooling rates of individual laser traces on IN625 bare plates. *Integr Mater Manuf Innov*. <https://doi.org/10.1007/s40192-020-00169-1>
- Zhang F, Levine LE, Allen AJ, Young SW, Williams ME, Stoudt MR et al (2019) Phase fraction and evolution of additively manufactured (AM) 15-5 stainless steel and Inconel 625 AM-Bench artifacts. *Integr Mater Manuf Innov* 8(3):362–377
- Phan TQ, Strantza M, Hill M, Gnaeupel-Herold TH, Heigel JC, D’Elia JC, DeWald AT, Clausen B, Pagan DC, Ko P, Brown DW, Levine LE (2019) Elastic residual strain and stress measurements and corresponding part deflections of 3D additive manufacturing builds of IN625 AM-Bench artifacts using neutron diffraction, synchrotron X-ray diffraction, and contour method. *Integr Mater Manuf Innov* 8(3):318–334
- Levine LE, Lane BM, Heigel JC, Migler K, Stoudt MR, Phan TQ, Ricker RE, Strantza M, Hill M, Zhang F, Seppala J, Garboczi E, Bain E, Cole D, Allen AJ, Fox J, Campbell CE (2020) Outcomes and conclusions from the 2018 AM-Bench measurements, challenge problems, modeling submissions, and conference. *Integr Mater Manuf Innov*. <https://doi.org/10.1007/s40192-019-00164-1>
- Heigel JC, Lane BM, Levine LE (2020) In situ measurements of melt-pool length and cooling rate during 3D builds of the metal AM-Bench artifacts. *Integr Mater Manuf Innov*. <https://doi.org/10.1007/s40192-020-00170-8>
- Levine LE, Stoudt MR, Lane BM (2018) A preview of the NIST/TMS additive manufacturing benchmark test and conference series. *JOM* 70:259–260

17. Levine LE (2018) Additive manufacturing benchmark test series. NIST. <https://www.nist.gov/ambench>. Accessed 2 Mar 2020
18. Anon (2019) Inconel (Wikipedia, The Free Encyclopedia). <https://en.wikipedia.org/w/index.php?title=Inconel&oldid=884478648>. Accessed 2 Mar 2020
19. Suave L, Cormier J, Villechaise P, Soula A, Hervier Z, Bertheau D, Laigo J (2014) Microstructural evolutions during thermal aging of alloy 625: impact of temperature and forming process. *Metall Mater Trans A* 45:2963–2982
20. Petrzak P, Kowalski K, Blicharski M (2016) Analysis of phase transformations in Inconel 625 alloy during annealing. *Acta Phys Pol A* 130:1041–1044
21. Sundaraman M, Kumar L, Prasad GE, Mukhopadhyay P, Banerjee S (1999) Precipitation of an intermetallic phase with Pt 2 Mo-type structure in alloy 625. *Metall Mater Trans A* 30:41–52
22. Cortial F, Corrieu JM, Vernot-Loier C (1995) Influence of heat treatments on microstructure, mechanical properties, and corrosion resistance of weld alloy 625. *Metall Mater Trans A* 26:1273–1286
23. Zhang F, Levine LE, Allen AJ, Stoudt MR, Lindwall G, Lass EA, Williams ME, Idell Y, Campbell CE (2018) Effect of heat treatment on the microstructural evolution of a nickel-based superalloy additive-manufactured by laser powder bed fusion. *Acta Mater* 152:200–214
24. Stoudt MR, Lass EA, Ng DS, Williams ME, Zhang F, Campbell CE, Lindwall G, Levine LE (2018) The influence of annealing temperature and time on the formation of δ -phase in additively-manufactured Inconel 625. *Metall Mater Trans A* 49:3028–3037
25. Lass EA, Stoudt MR, Williams ME, Katz MB, Levine LE, Phan TQ, Gnaeupel-Herold TH, Ng DS (2017) Formation of the Ni_3Nb_8 -phase in stress-relieved Inconel 625 produced via laser powder-bed fusion additive manufacturing. *Metall Mater Trans A* 48:5547–5558
26. Lass EA, Stoudt MR, Katz MB, Williams ME (2018) Precipitation and dissolution of δ and γ “during heat treatment of a laser powder-bed fusion produced Ni-based superalloy”. *Scr Mater* 154:83–86
27. VanderVoort GF (1999) *Metallography principles and practice*. ASM International, Materials Park
28. Keller T, Lindwall G, Ghosh S, Ma L, Lane BM, Zhang F, Kattner UR, Lass EA, Heigel JC, Idell Y, Williams ME, Allen AJ, Guyer JE, Levine LE (2017) Application of finite element, phase-field, and CALPHAD-based methods to additive manufacturing of Ni-based superalloys. *Acta Mater* 139:244–253
29. Zhang F, Levine LE, Allen AJ, Campbell CE, Lass EA, Cheruvathur S, Stoudt MR, Williams ME, Idell Y (2017) Homogenization kinetics of a nickel-based superalloy produced by powder bed fusion laser sintering. *Scr Mater* 131:98–102
30. Hielscher R, Schaeben H (2008) A novel pole figure inversion method: specification of the MTEX algorithm. *J Appl Cryst* 41:1024–1037
31. Mason JK, Schuh JK (2009) Representations of texture. In: Schwartz AJ, Kumar M, Adams BL, Field DP (eds) *Electron back-scattered diffraction in materials science*. Springer, New York, pp 35–51
32. Piglione A, Dovgvy B, Liu C, Gourlay CM, Hooper PA, Pham MS (2018) Printability and microstructure of the CoCrFeMnNi high-entropy alloy fabricated by laser powder bed fusion. *Mater Lett* 224:22–25